AGU PUBLICATIONS

JGR

Journal of Geophysical Research: Oceans

RESEARCH ARTICLE

10.1002/2014JC009993

Companion to *King et al.* [2015], doi:10.1002/2014JC009992.

Key Points:
- Third-order structure function analysis in the tropical Pacific
- Direction of the turbulent energy cascade varies with region and month
- Results from ASCAT and QuikSCAT scatterometer ocean winds are in excellent agreement.

Correspondence to:
J. Vogelzang,
jur.vogelzang@knmi.nl

Citation:
King, G. P., J. Vogelzang, and A. Stoffelen (2015), Upscale and downscale energy transfer over the tropical Pacific revealed by scatterometer winds, *J. Geophys. Res. Oceans*, *120*, 346–361, doi:10.1002/2014JC009993.

Received 24 MAR 2014
Accepted 13 AUG 2014
Accepted article online 23 DEC 2014
Published online 28 JAN 2015

Upscale and downscale energy transfer over the tropical Pacific revealed by scatterometer winds

Gregory P. King[1,2,3,4], Jur Vogelzang[5], and Ad Stoffelen[5]

[1]School of Marine Sciences, Nanjing University of Information Science and Technology, Nanjing, China, [2]Centro de Geofisica—IDL, Campo Grande, Edificio 8, Universidade de Lisboa, Lisboa, Portugal, [3]Instituto Gulbenkian de Ciencia, Oeiras, Portugal, [4]Institute of Marine Sciences (ICM-CSIC), Passeig Marítim Barceloneta, Barcelona, Spain, [5]Royal Netherlands Meteorological Institute, De Bilt, Netherlands

Abstract The direction of the energy cascade in the mesoscales of atmospheric turbulence is investigated using near-surface winds over the tropical Pacific measured by satellite scatterometers SeaWinds (QuikSCAT) and ASCAT (MetOp-A). The tropical Pacific was subdivided into nine regions, classified as rainy or dry. Longitudinal third-order along-track structure functions D_{LLLa} and skewness S_{La} were calculated as a function of separation r for each region and month during the period November 2008 to October 2009. We find that the results support both downscale and upscale interpretations, depending on region and month. The results indicate that normally energy cascades downscale, but cascades upscale over the cold tongue in the cold season and over the west Pacific in summer months. An explanation is offered based on the heating or cooling of the air by the underlying sea surface temperature. It is also found that the signature of intermittent small-scale ($<$100 km) events could be identified in graphs of S_{La}, implying that this diagnostic may be useful in the studies of tropical disturbances.

1. Introduction

Is horizontal kinetic energy transferred to small scales through a downscale cascade as in three-dimensional (3-D) turbulence? Or is it transferred to large scales via a two-dimensional (2-D) upscale cascade? This long-standing question in atmospheric dynamics is addressed here using near-surface winds over the tropical Pacific measured from space by the Advanced Scatterometer (ASCAT) on the MetOp-A satellite and the SeaWinds scatterometer on the QuikSCAT satellite.

In a classic paper, *Nastrom et al.* [1984] demonstrated that horizontal wavenumber spectra calculated for winds measured near the tropopause follow a $k^{-5/3}$ power law at small scales (between 2 and 300–400 km) and a k^{-3} power law at large scales (more recently argued to be closer to $k^{-2.4}$) [*Lovejoy et al.*, 2009]. These scaling laws were found to vary little with region and season [*Nastrom and Gage*, 1985]. The k^{-3} range is consistent with the theory of quasi-geostrophic turbulence [*Charney*, 1971]. The origin of the $k^{-5/3}$ range, however, continues to be debated. Two types of theories have been put forth: one based on internal gravity wave dynamics and the other on stratified turbulence.

The gravity wave scenario predicts a downscale cascade of energy from longer to shorter waves [*Dewan*, 1979; *Van Zandt*, 1982; *Dewan*, 1997]. On the other hand, geophysical constraints (stratification, rotation, thin atmosphere) decouple atmospheric motions into layers, motivating the picture of stratified turbulence with energy sources at large scale (e.g., baroclinic instability) and small scale (e.g., convection and shearing instabilities). This scenario predicts an upscale cascade of energy [*Gage*, 1979; *Lilly*, 1983, 1989].

After repeated efforts to use wavenumber spectra to distinguish between the gravity wave and stratified turbulence scenarios were unsuccessful, *Lindborg* [1999] proposed a new approach based on the most fundamental result in turbulence theory—the Kolmogorov *four-fifths law*: $D_{LLL} = -\frac{4}{5}\varepsilon_3 r$. Here $D_{LLL} = \langle(\delta u_L)^3\rangle$ is the third-order longitudinal structure function, δu is the velocity difference at scale r in the direction parallel with $\mathbf{r}$, and ε_3 is the energy dissipation rate (energy flux) for 3-D turbulence. Reworking the Kolmogorov analysis for 2-D turbulence, Lindborg deduced that $D_{LLL} = -\frac{3}{2}\varepsilon_2 r$, with the sign of ε_2 indicating the direction of the cascade; that is, if $D_{LLL} < 0$ energy is transferred downscale and if $D_{LLL} > 0$ energy is transferred upscale.

© 2014. American Geophysical Union. All Rights Reserved.

Cho and Lindborg [2001] calculated third-order structure functions using a data set of global aircraft winds measured near the tropopause. They found that in the small to intermediate scales, $D_{LLL} < 0$, implying a downscale energy cascade. Although this was consistent with the gravity wave scenario, *Lindborg* [2007] argued against it, proposing instead a stratified-downscale scenario wherein atmospheric layers created in stratified turbulence become unstable (e.g., by shear instability) and break up into smaller structures.

It is important to determine the generality of the *Cho and Lindborg* result. Is it true in all regions, seasons, and levels of the atmosphere? There are some reports already published identifying particular situations where the third-order structure function changes sign at different altitudes: in clear air turbulence [*Lu and Koch*, 2008] and in a tropical cyclone [*Byrne and Zhang*, 2013]. The work reported here provides further and more extensive evidence from the marine boundary layer using winds measured by ASCAT and QuikSCAT.

The paper is structured as follows. Structure functions are defined in section 2. The data, study area (tropical Pacific), and methodology are described in section 3. The results are presented in section 4 for the period November 2008 to October 2009 when both scatterometers were operational, and for the scale range 50–300 km where scatterometers identify small-scale structure not found in global numerical weather prediction forecast winds. Our conclusions are given in section 5.

2. Structure Functions

Structure functions are moments of the probability distribution function (PDF) of velocity differences $P_r(\delta\mathbf{u})$, where the subscript r denotes the separation distance, $\delta\mathbf{u}=(\delta u_L, \delta u_{1T}, \delta u_{2T})$ and $\delta u_j = u_j(x_L+r, x_{1T}, x_{2T}) - u_j(x_L, x_{1T}, x_{2T})$. The subscript L (T) stands for longitudinal (transverse), the component parallel (perpendicular) to the coordinate x_L. For isotropic turbulence, the two transverse directions become statistically equivalent so that we write $\delta u_T = \delta u_{1T} = \delta u_{2T}$.

The width of velocity difference PDFs are measured by the second-order structure functions

$$D_{LL}(r)=\langle \delta u_L \delta u_L \rangle, \quad D_{LT}(r)=\langle \delta u_L \delta u_T \rangle, \quad D_{TT}(r)=\langle \delta u_T \delta u_T \rangle, \tag{1}$$

and their deviation from symmetry by the third-order structure functions

$$D_{LLL}(r)=\langle \delta u_L (\delta u_L)^2 \rangle, \tag{2a}$$

$$D_{LTT}(r)=\langle \delta u_L (\delta u_T)^2 \rangle, \tag{2b}$$

where $\langle . \rangle$ denotes an ensemble average.

Deriving $P_r(\delta\mathbf{u})$ directly from the Navier-Stokes equations has met with limited success [*Giles*, 1997; *Yakhot*, 1999]. More successful has been derivations for second-order and third-order structure functions. The derivations use simplifications based on symmetry and other approximations [cf., *Lindborg and Cho*, 2001]. For example, isotropy implies $D_{LT}(r)=0$, which together with the assumption of divergence-free turbulence yields [cf., *Landau and Lifshitz*, 1987]

$$D_{TT}(r)=D_{LL}(r)+\frac{r}{d-1}\frac{d}{dr}D_{LL}(r), \tag{3}$$

$$D_{LTT}(r)=\frac{r}{3}\frac{d}{dr}D_{LLL}(r), \tag{4}$$

where $d=2$ and $d=3$ for 2-D and 3-D turbulence, respectively. These assumptions also lead to the third-order structure function laws

$$D_{LLL}=-\kappa_{Ld}\varepsilon_d r, \tag{5a}$$

$$D_{LTT}=-\kappa_{Td}\varepsilon_d r, \tag{5b}$$

where ε_d is the energy dissipation, $(\kappa_{L2}, \kappa_{T2})=(\frac{3}{2}, \frac{1}{2})$, and $(\kappa_{L3}, \kappa_{T3})=(\frac{4}{5}, \frac{4}{15})$ [*Antonia et al.*, 1997; *Lindborg and Cho*, 2001]. The key difference is that the energy flux is downscale ($\varepsilon_3 > 0$) in 3-D turbulence, but upscale ($\varepsilon_2 < 0$) in 2-D turbulence [*Lindborg*, 1999].

© 2014. American Geophysical Union. All Rights Reserved.

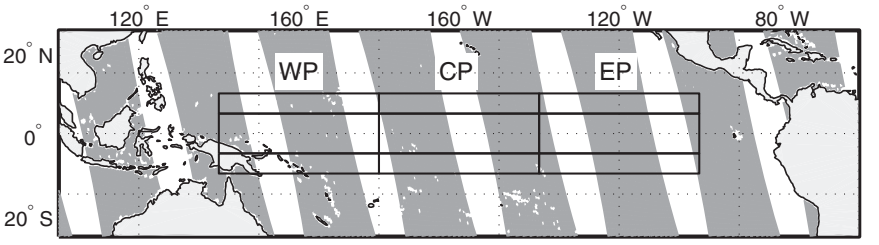

Figure 1. The boundaries of the nine geographical regions studied in this paper. The nomenclature and geographical limits are given in Table 1. Some SeaWinds ascending swaths are shown in gray.

The normalized third-order moment or skewness quantifies the asymmetry of the underlying PDF. Often studied is the longitudinal skewness

$$S_L(r) = \frac{D_{LLL}(r)}{D_{LL}^{3/2}(r)}. \tag{6}$$

If the turbulence follows the classical Kolmogorov scaling

$$D_{LL}(r) = C_d |\varepsilon_d|^{2/3} r^{2/3}, \tag{7}$$

then $S_L(r)$ reduces to a constant, given by

$$S_{Ld} = -\frac{\mathrm{sgn}(\varepsilon_d)\kappa_{Ld}}{C_d^{3/2}}. \tag{8}$$

Using $C_2 \approx 12.9$ [*Boffetta et al.*, 2000; *Boffetta and Ecke*, 2012] and $C_3 \approx 2$ [*Frisch*, 1995, p. 90], the skewness for 2-D turbulence is

$$S_{L2} = \frac{3/2}{C_2^{3/2}} \approx 0.03, \tag{9a}$$

indicating that the PDF $P_r(\delta u_L)$ has a small positive skewed shape, and the skewness for 3-D turbulence is

$$S_{L3} = \frac{-4/5}{C_3^{3/2}} \approx -0.28, \tag{9b}$$

indicating $P_r(\delta u_L)$ is negatively skewed.

3. Data, Study Area, and Methodology

3.1. Data

The QuikSCAT satellite was launched by the National Aeronautics and Space Administration (NASA) in June 1999. The mission produced ocean vector winds from July 1999 to November 2009. The MetOp-A satellite was launched in October 2006 and is operated by the European Organisation for the Exploitation of Meteorological Satellites (EUMETSAT). Both satellites are in quasi sun-synchronous orbits with an inclination angle of $\theta = 98.6°$. The local times for crossing the equator are about 06:30 (ascending) and 18:30 (descending) for QuikSCAT, and about 09:30 (descending) and 21:30 (ascending) for MetOp-A.

The SeaWinds-on-QuikSCAT scatterometer is a rotating pencil-beam design with an 1800 km wide swath, transmitting at Ku-band (13.4 GHz) [*Tsai et al.*, 2000]. The pencil-beam design has a complicated observation geometry that varies across the swath, resulting in a varying performance that is poor in the nadir region and far swath. The ASCAT-on-MetOp-A scatterometer uses a dual-swath fan-beam configuration with two 550 km wide swaths separated by a nadir gap of about 700 km, transmitting at C-band (5.3 GHz) [*Figa-Saldaña et al.*, 2002]. The fan-beam configuration has constant measurement geometry but varying incidence angle over the swath.

The data are the same as used in *King et al.* [2015], where they are described in more detail. Briefly, we use (i) *ASCAT-12.5*, a 12.5 km product, and (ii) *ASCAT-25*, a 25 km product, both produced by the Royal

© 2014. American Geophysical Union. All Rights Reserved.

Table 1. Geographical Limits and Nomenclature for the Study Regions Shown in Figure 1

	West Pacific 140°E–180°E	Central Pacific 180°E–220°E	East Pacific 220°E–260°E
North 5°N–10°N	WPN (rainy)	CPN (rainy)	EPN (rainy)
Equatorial 5°S–5°N	WPE (rainy)	CPE (dry)	EPE (dry)
South 10°S–5°S	WPS (rainy)	CPS (dry)	EPS (dry)

Netherlands Meteorological Institute (KNMI); (iii) *SeaWinds-NOAA*, a 25 km near-real-time product issued by the National Oceanic and Atmospheric Administration (NOAA); (iv) *SeaWinds-KNMI*, a reprocessing of SeaWinds-NOAA by KNMI using improved (rain) quality control [*Portabella and Stoffelen*, 2002]; (v) *QSCAT-12.5* (version 3), a reprocessed 12.5 km product from the NASA Jet Propulsion Laboratory (JPL) containing many algorithm improvements [*Fore et al.*, 2013].

Ambiguity removal is carried out for the two ASCAT and the SeaWinds-KNMI products using a two-dimensional variational method (2-DVAR) [*Vogelzang et al.*, 2009]. The SeaWinds-KNMI product is also processed using additional noise reduction by the Multiple Solution Scheme (MSS) [*Vogelzang et al.*, 2009]. Ambiguity removal is carried out for the SeaWinds-NOAA and QSCAT-12.5 products using a median filter followed by a sophisticated algorithm called Direction Interval Retrieval with Thresholded Nudging (DIRTH) [*Stiles et al.*, 2002] (with improvements applied in the QSCAT-12.5 processing).

Environmental conditions are characterized using rain-rates from the Tropical Rainfall Measuring Mission's (TRMM) Microwave Imager (TMI) on board the TRMM satellite and the SeaWinds Radiometer (SRAD) rain-rates (derived from ocean radiometric brightness temperature) [*Laupattarakasem et al.*, 2005]. The TMI data were obtained from Remote Sensing Systems (http://www.ssmi.com), and the SRAD rain-rates were obtained from the QuikSCAT 25 km L2B science data product (available from the Physical Oceanography Distributed Data Archive (PO.DAAC)).

The main spatial processing differences that are expected to affect the third-order structure function results are:

1. Scatterometer geometry and related ambiguity removal filtering (AR); QuikSCAT geometry is more complicated than ASCAT, and hence so too is ambiguity removal, where small-scale spatial structure is clearly affected [*Stoffelen and Portabella*, 2006; *Portabella and Stoffelen*, 2004]. For ASCAT spatial effects due to AR are thought to be negligible.
2. Backscatter data are averaged locally and the fundamental footprints extend the averaging box, called wind vector cell (WVC). This implies spatial filtering and noise reduction closely following Nyquist sampling, but may cause correlated noise in neighboring WVCs (only at lag 1).
3. Rain affects radar backscatter; it is potentially a large source of error for winds derived from Ku-band instruments (SeaWinds) and small for C-band instruments (ASCAT) [*Lin et al.*, 2014].

The precise effect of these instrument and processing differences (and errors introduced by them) on third-order structure functions is variable and hard to estimate in advance. Therefore, results will be presented for the five wind products mentioned earlier in order to be able to detect such effects.

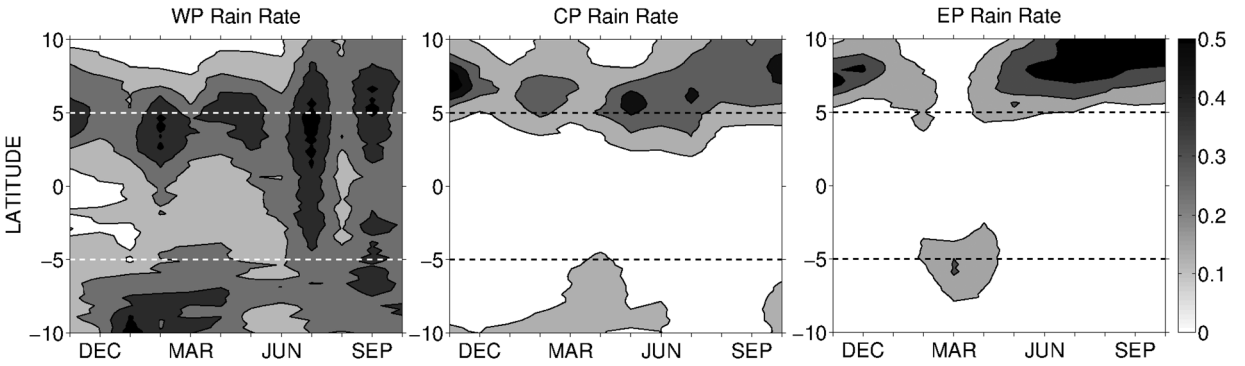

Figure 2. Latitude-time plots of monthly and zonally average rain-rate measured by the TRMM Microwave Imager (TMI) during the study period November 2008 to October 2009.

© 2014. American Geophysical Union. All Rights Reserved.

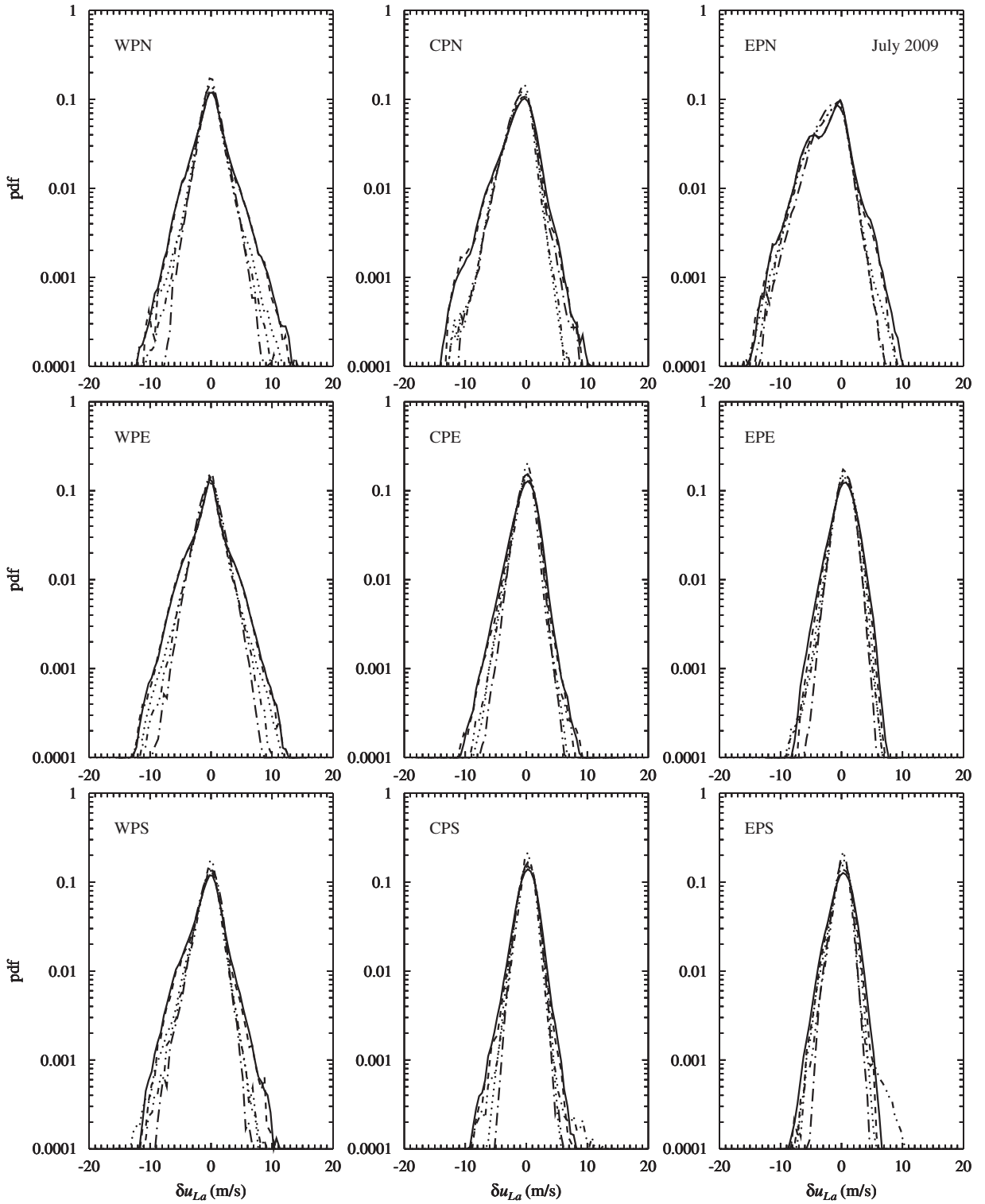

Figure 3. Probability distributions of velocity increments δu_{La} at separation $r = 200$ km for July 2009. Solid curves: ASCAT-12.5, dashed curves: ASCAT-25, dot-dashed curves: SeaWinds-KNMI, dot-dot-dashed curves: SeaWinds-NOAA, and dotted curves: QSCAT-12.5.

3.2. Study Area

The study area is shown in Figure 1 and is the same as used in *King et al.* [2015]. The area is bounded by latitudes 10°S and 10°N and longitudes 140°E and 260°E and is divided into three latitude bands (North,

© 2014. American Geophysical Union. All Rights Reserved.

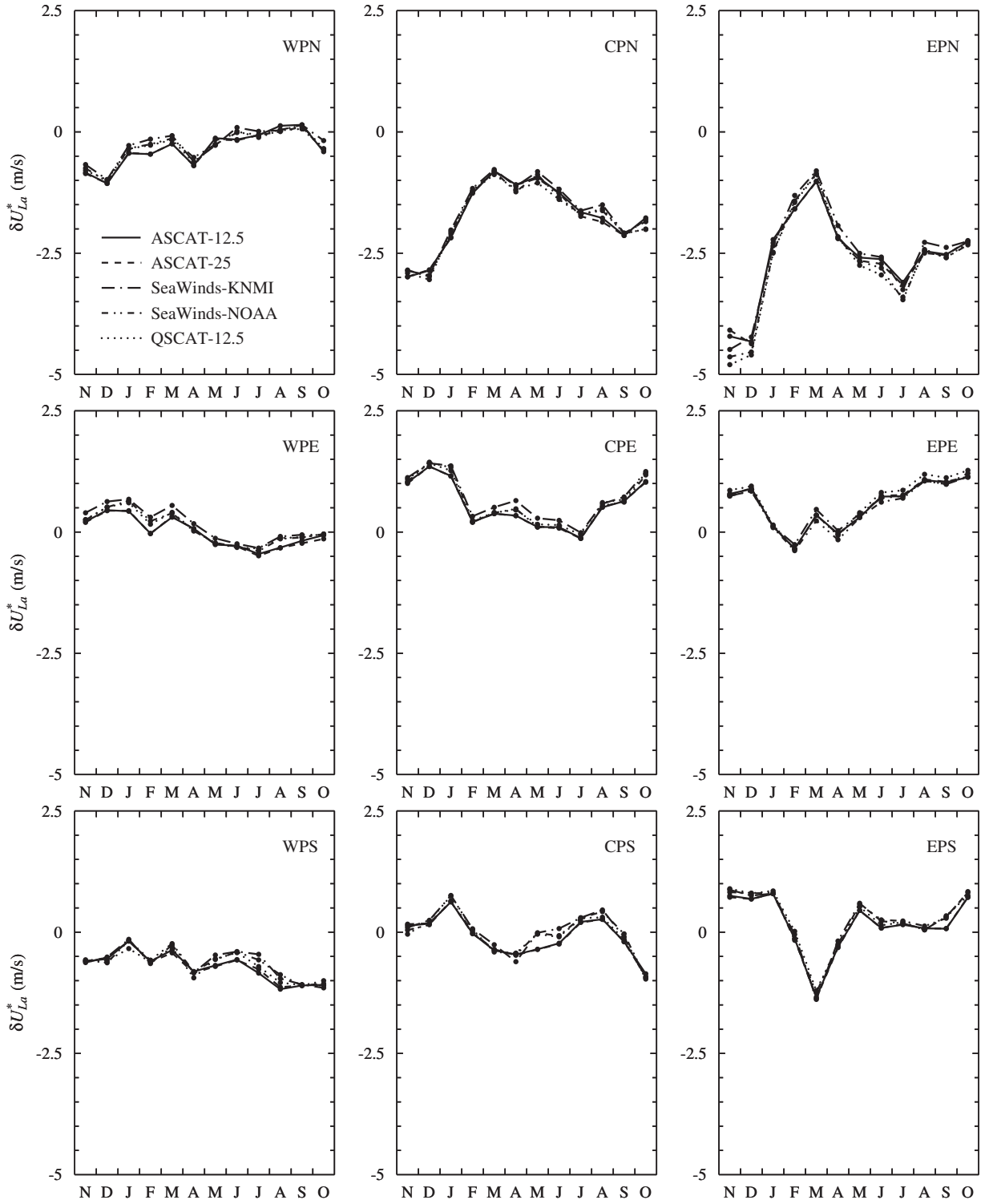

Figure 4. Time series of the mean of the PDF, δU^*_{La}, at separation $r = 300$ km. The regional and seasonal complexity of δU^*_{La} reflects the divergent and convergent characteristics of the large-scale mean flow induced by the warm pools, convergence zones, and SST fronts in the tropical Pacific.

Equatorial, South) and three longitude bands (West, Central, and East Pacific), as indicated in Figure 1 and Table 1. Figure 2 shows latitude-time plots of rain-rate for the study period. The rainy regions contain the west Pacific warm pool (WPN, WPE, WPS), the South Pacific Convergence Zone (WPS), and the Inter-Tropical Convergence Zone or ITCZ (CPN, EPN). The warm pool is defined as the waters enclosed

© 2014. American Geophysical Union. All Rights Reserved.

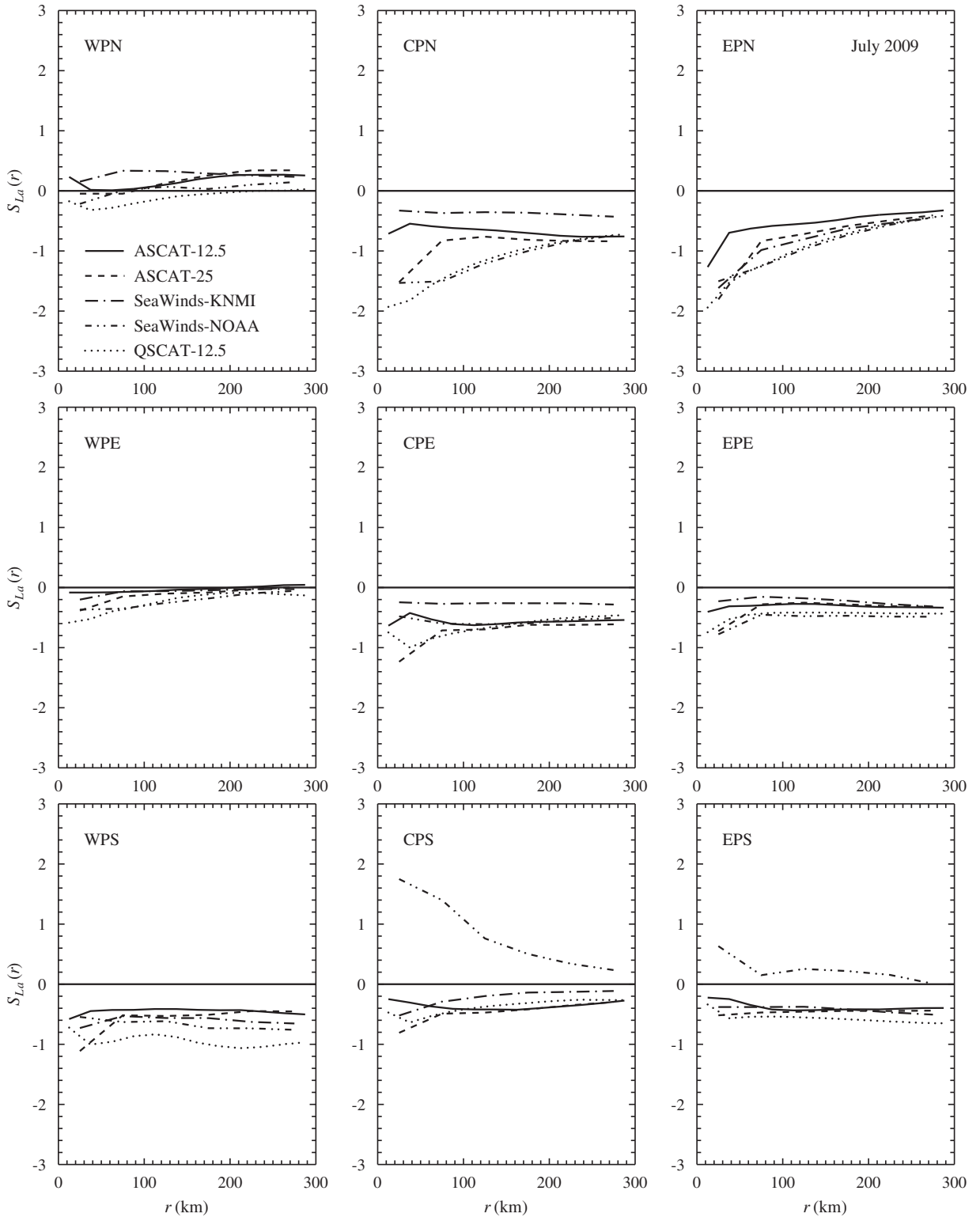

Figure 5. The longitudinal skewness $S_{La}(r)$ for all wind products and regions for July 2009.

by the 28°C isotherm [*Wyrtki*, 1989], an empirical threshold for the onset of deep convection. The low rainfall in the dry regions (CPE, EPE, CPS, EPS) is due to a tongue of cool water brought to the surface by upwelling-favorable winds along South America. Due to southerly winds blowing from cool to warm

© 2014. American Geophysical Union. All Rights Reserved.

ocean waters across the strong SST front that forms the northern boundary of the east Pacific cold tongue [*Chelton et al*., 2004; *Small et al*., 2008, and references therein], EPE is a region of strong surface divergence. As Figure 2 shows, the dry zones also have wet months. See *King et al*. [2015] for further discussion of the study area.

3.3. Methodology

Samples were selected along-swath: wind vector cells in the same sample all have the same cross-swath index. Each sample was checked to ensure that wind vectors falling outside the subregion of interest or failing quality control were flagged missing. In the case of SeaWinds-NOAA and QSCAT-12.5, wind vectors were flagged missing if the rain flag was set. In the case of ASCAT and SeaWinds-KNMI, wind vectors were flagged missing if the KNMI quality control flag or the variational quality control flag was set [*KNMI*, 2013, section 6.2]. Samples from both the ascending and descending passes of the satellite and from the whole swath (including the outer and nadir parts of the SeaWinds swath) were used to calculate the structure functions.

Velocity differences are taken between members of each along-track sample after transforming wind vectors into components parallel (u_{La}) and perpendicular (u_{Ta}) to the satellite track, as indicated by the subscript *a*.

We focus on the scale range 50–300 km. This is the range where scatterometer winds contain more kinetic energy variance than global NWP forecast winds. Moreover, these are the scales occupied by mesobeta weather phenomena such as squall lines and mesoscale convective systems, adding importance to this choice.

Empirical velocity increment PDFs $P_r(\delta u_{La})$ were constructed using all $\delta u_{La}(r,t)$ during a calendar month per region and per wind product for each separation *r*. As emphasized by *Xia et al*. [2009], the presence of a large-scale mean flow will contaminate structure functions calculated via a straight-forward application of equations (1) and (2). This is avoided by first calculating the mean

$$\delta U_{La}(r)=\sum_{\delta u_{La}} \delta u_{La} P_r(\delta u_{La}), \tag{10a}$$

and then using the centered PDF to compute:

$$D_{LLa}(r)=\sum_{\delta u'_{La}} \left(\delta u'_{La}\right)^2 P_r\left(\delta u'_{La}\right), \tag{10b}$$

$$D_{LLLa}(r)=\sum_{\delta u'_{La}} \left(\delta u'_{La}\right)^3 P_r\left(\delta u'_{La}\right), \tag{10c}$$

where $\delta u'_{La}(r)=\delta u_{La}(r)-\delta U_{La}(r)$.

3.4. Accuracy

Vogelzang et al. [2011] show that the scatterometer zonal and meridional wind components, *u* and *v*, have an accuracy of about 0.7 m/s (at the 1-σ level). The same accuracy holds for the along-track and cross-track components, *L* and *T*, so $\Delta L \approx 0.7$ m/s. The error variance in the difference δL_a is estimated twice as large, so $\Delta(\delta L_a) \approx 14.0$ m/s. The error in the third power of the velocity difference is that value to the third power, so $\Delta(\delta L_a)^3 \approx 1.0$ m^3/s^3. Finally, the error in the third-order structure function is $\Delta D_{LLLa} \approx 1.0\, N^{-1/2}$ m^3/s^3, with *N* the number of differences averaged over.

The value of *N* differs per lag, per region, and per wind product. Most pairs are found for small lags, while only a few pairs are found for the largest lags presented in the next section. The equatorial longitude bands are twice as large as the northern and southern bands. ASCAT-12.5 has half the grid size as the other products, so it has four times as many points in a given region and a given period.

For lag size 1, the value of *N* ranges for July 2009 from 729,249 (ASCAT-12.5 in EPE) to 61,811 (ASCAT-25 in WPS), so ΔD_{LLLa} ranges from 0.001 to 0.004 m^3/s^3. For a range of 300 km, the value of *N* ranges from 529,290 (ASCAT-12.5 in EPE) to 22,574 (ASCAT-25 in WPS), so ΔD_{LLLa} ranges from

© 2014. American Geophysical Union. All Rights Reserved.

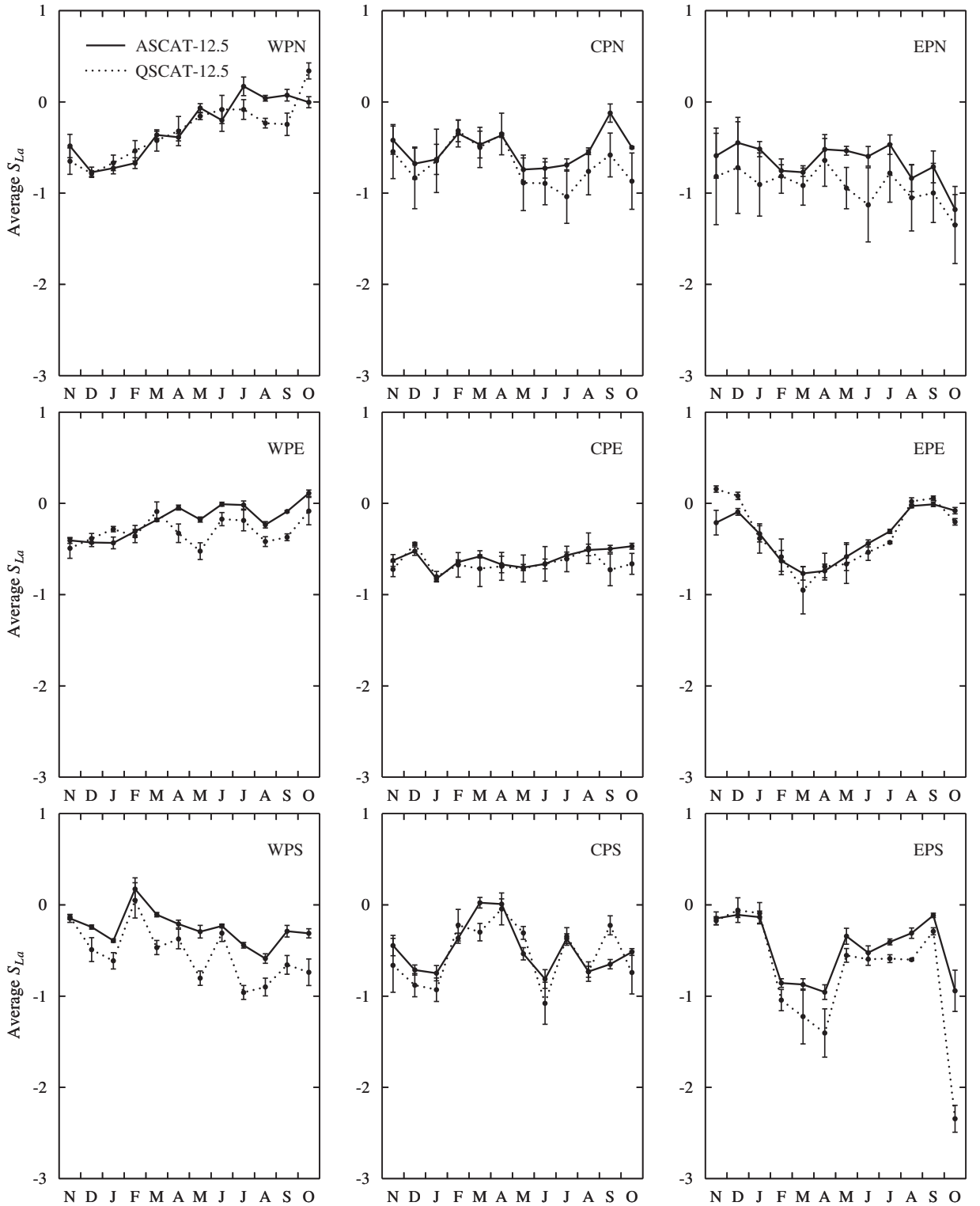

Figure 6. Time series of the average longitudinal skewness $\overline{S_{La}}$. Error bars show the root-mean-square deviation from the average. Large error bars indicate the presence of strong trends (see EPN in Figure 4).

0.002 to 0.008 m^3/s^3. It is therefore safe to say that the errors in the results shown in the next section are negligible with respect to the scale of the figures, except for the last points at the highest lags.

© 2014. American Geophysical Union. All Rights Reserved.

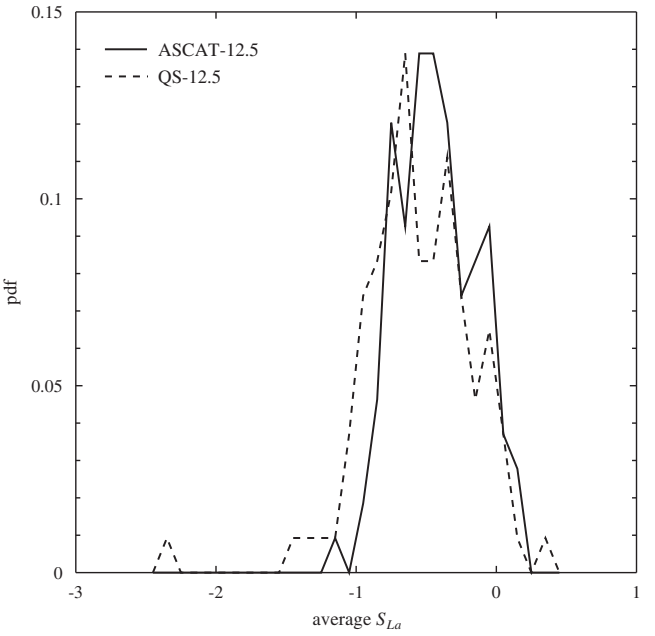

Figure 7. Normalized histogram of the average skewness $\overline{S_{La}}$.

4. Results

Figure 3 shows empirical PDFs at scale $r = 200$ km for the month July 2009. The PDFs are plotted on a logarithmic scale, which shows that the tails are exponential. Results for five wind products are shown: ASCAT-12.5 (solid curves), ASCAT-25 (dashed curves), SeaWinds-KNMI (dot-dashed curves), SeaWinds-NOAA (dot-dot-dashed curves), and QSCAT-12.5 (dotted curves). The PDFs reveal some systematic differences between wind products. SeaWinds PDFs always fit within ASCAT PDFs (except for SeaWinds-NOAA in CPS and EPS), indicating that they have less variance. The difference in variance is much larger in rainy than dry regions, implying that the missing variance can be attributed, at least in part, to rejection of rain-contaminated winds. However, it can also be attributed to the spatial AR filtering inherent in the more complicated SeaWinds observation geometry.

To determine the source of the outliers in the long positive tail of the SeaWinds-NOAA PDFs for CPS and EPS, the SeaWinds-NOAA swath fields were searched for cases where $\delta u_{La} > 5$ m/s. From the search, it was discovered that ambiguity retrieval errors in the outer swath cause an almost 90° difference in wind direction over short distances. The SeaWinds-KNMI product does not have these outliers because the reprocessing of the NOAA data used here did not use retrievals from that part of the swath.

Also note that the "shoulders" and "wiggles" in the ASCAT PDFs in the rainy regions. Such features are not apparent in SeaWinds PDFs. Further work is needed to understand the source of these features.

The tropical Pacific has a mean flow that varies regionally and seasonally due to changes in location and spatial extent of the west Pacific warm pool, east Pacific cold tongue, and the convergence zones (ITCZ, SPCZ, and S-ITCZ). This variability is reflected in the mean values, $\delta U_{La}(r)$, of the PDFs. A review of graphs of $\delta U_{La}(r)$ for all PDFs in each region and each month shows that the mean varies as $\delta U_{La} = Ar$, where the slope, A, varies in sign and magnitude as a function of region and month. Due to the simple dependence on r, it suffices to represent the variability of δU_{La} using its value at $r = 300$ km. This is shown in Figure 4, which emphasizes and portrays the divergent and convergent characteristics of the large-scale mean flow induced by the warm pools, convergence zones, and SST fronts in the tropical Pacific (compare with Figure 2 and Figure 1 in *King et al.* [2015]).

The longitudinal skewness, $S_{La} = D_{LLLa}/D_{LLa}^{3/2}$, quantifies PDF asymmetry as a function of scale. Graphs of $S_{La}(r)$ for July 2009 are shown in Figure 5. Ignoring the graphs for SeaWinds-NOAA in CPS and EPS (which are contaminated by artifacts), the remaining graphs can be roughly described as close to one of two types. Type 1 represents ideal inertial-range turbulence, where S_{La} equals an r-independent constant that depends on the dimensionality of the turbulence. Type 2 represents turbulence with scale interactions: at small scales S_{La} is large negative, transitioning to the Type 1 graph with increasing scale.

Figure 5 shows that most graphs are similar to Type 1. The constant varies within the range $(-0.5, 0.5)$, which compares favorably with the range $(-0.3, 0.03)$ set by ideal 3-D and 2-D turbulence. The graphs for EPN are closer to the scale interaction type: S_{La} is large-negative at small r, and then increases, asymptotically approaching a less negative value at large r. The graphs for CPN do not lend themselves to a consistent interpretation. For example, ASCAT-12.5 S_{La} is Type 1, but ASCAT-25 is Type 2—implying that S_{La} at

© 2014. American Geophysical Union. All Rights Reserved.

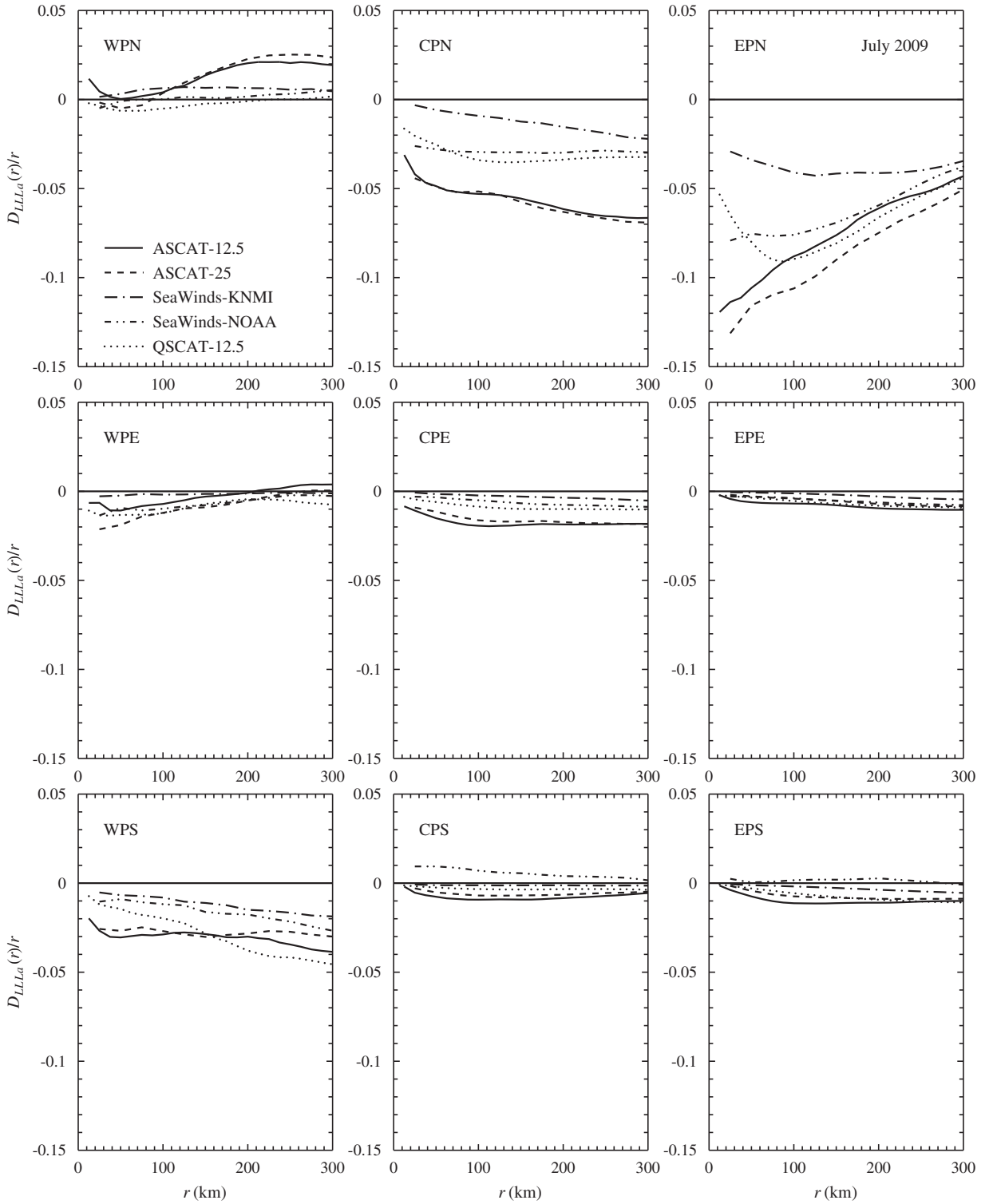

Figure 8. Normalized third-order structure functions D_{LLLa}/r versus r. Graphs are for July 2009.

small r can be sensitive to methods used to process the radar backscatter. Therefore, an additional check was carried out to aid in the interpretation of the CPN and EPN results. A visual review of QuikSCAT vector wind fields for the tropical Pacific on a swath-by-swath basis for the July 2009 period using the browsing facility on the Remote Sensing Systems web site revealed clusters of spatially localized concentrations of

© 2014. American Geophysical Union. All Rights Reserved.

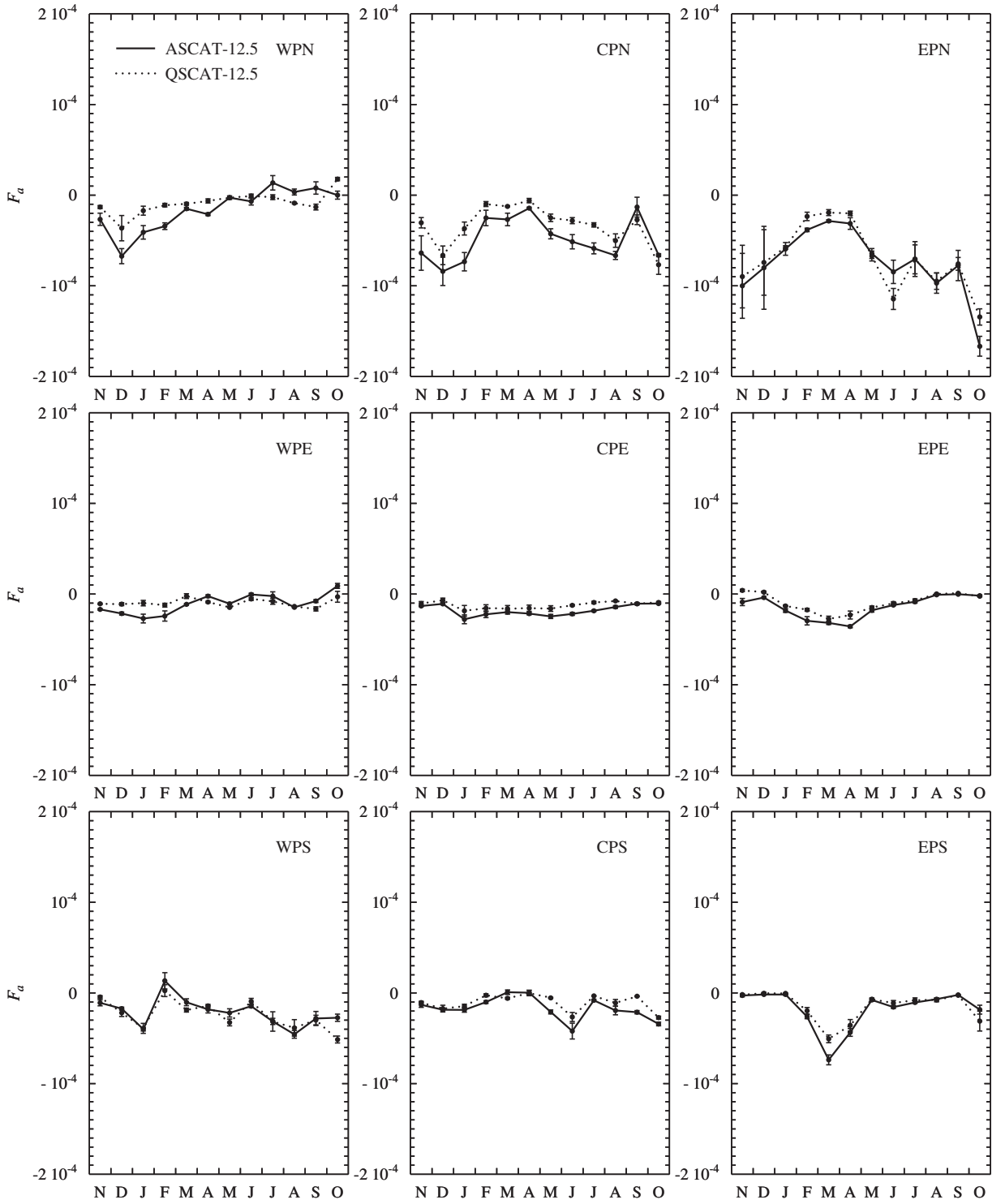

Figure 9. Time series of the energy flux F_a (units of 10^{-4} m^2 s^{-3}). Fluxes are estimated using the third-order structure function law (equation (5)).

high kinetic energy (on scales up to about 100 km) propagating westward along the axis of the ITCZ first through EPN and then through CPN. The clusters are believed to be the signature of strong convective activity. Convective activity implies convergent horizontal winds and hence implies these clusters are the source of large negative S_{La} for scales less than about 100 km.

© 2014. American Geophysical Union. All Rights Reserved.

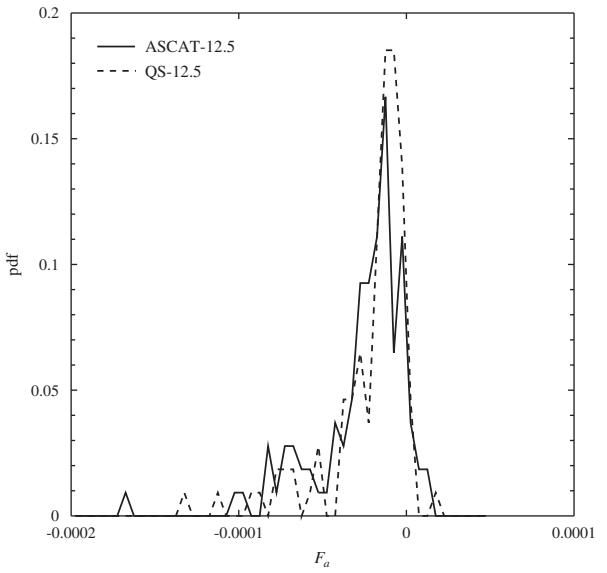

Figure 10. Normalized histograms of the energy flux F_a (units of 10^{-4} m^2 s^{-3}).

Figure 6 shows monthly time series of S_{La}, the mean value for the interval 50–300 km. Results for all wind products are similar, but for clarity, only results for ASCAT-12.5 and QSCAT-12.5 are shown. The figure shows that the two wind products are in broad agreement. The error bars (root-mean square deviations) are large when the graph of $S_{La}(r)$ exhibits large trends. A review of results for all months and regions confirmed that large error bars correspond to graphs of $S_{La}(r)$ similar to those for EPN shown in Figure 5. Note that the QSCAT product has more large error bars than ASCAT. This is likely the result of sampling differences due to different satellite crossing times (MetOp-A and QuikSCAT pass over the same region at different times of the day) and because ASCAT has a nadir gap, but QuikSCAT does not.

Figure 7 shows the distribution of S_{La} (obtained by pooling the results for each wind product separately in Figure 6) for ASCAT-12.5 and QSCAT-12.5. The peaks of the two distributions are slightly different, but otherwise fill the interval $(-1, 0.2)$. This provides strong support for the interpretation that mesoscales turbulence in the marine boundary layer can be either 3-D-like or 2-D-like.

If in accord with 2-D or 3-D turbulence theory, third-order structure functions normalized by r will yield straight horizontal lines (equation (5)). Figure 8 shows that the graphs of D_{LLLa}/r are either approximately straight horizontal lines or tend to that at large r (i.e., by about 200 – 300 km). Let F_a denote the mean of D_{LLLa}/r calculated over the interval 50–300 km. Time series of F_a for the ASCAT-12.5 and QSCAT-12.5 products are shown in Figure 9; the error bars indicate the root-mean-square deviation. Figure 10 shows the normalized histograms obtained after pooling results from all regions and months. Calculating the mean over different ranges (e.g., 200–300 km) made little difference. Using relation (5a), the mean of the distribution(s) converts to a mean dissipation rate $\varepsilon \approx 2\times 10^{-5}$ m^2 s^{-3}, a value consistent with dissipation rates estimated from aircraft measurements by *Cho et al.* [2001] and *Lindborg and Cho* [2001].

As a validation and self-consistency check, we estimate the Kolmogorov constant using the constants for 3-D turbulence. Using (7), we write $C_{3La}=D_{LLa(r)}/|\varepsilon_a r|^{2/3}$, where $\varepsilon_a=\frac{5}{4}|F_a|$ and (10b) is used to calculate $D_{LLa}(r)$. Figure 11 shows the times series and Figure 12 shows the normalized histogram of C_{3La} for ASCAT-12.5 and QSCAT-12.5. Most values lie between 1 and 2, which compares well with the accepted value $C_{3L} \approx 2$ [*Frisch*, 1995, p. 90]. The larger values of C_{3La} are consistent with the flow in a state of 2-D turbulence—or intermediate between 2-D and 3-D turbulence—and give confidence in the methodology and results presented in this paper.

5. Conclusions

The objective of this paper was to determine if the turbulence in the ocean wind field was more like 3-D or more like 2-D turbulence. This was investigated using data sets of ocean vector winds measured by the SeaWinds (on QuikSCAT) and ASCAT (on MetOp-A) scatterometers over the tropical Pacific during a 12 month period when both instruments were operational. Five wind products were compared (two ASCAT and three SeaWinds), giving increased confidence in the results. The wind products were all Level 2B winds.

Velocity differences were formed and used to construct empirical PDFs for both rainy and dry regions. From the PDFs, third-order structure functions D_{LLLa} and skewness S_{La} were calculated as a function of separation r.

© 2014. American Geophysical Union. All Rights Reserved.

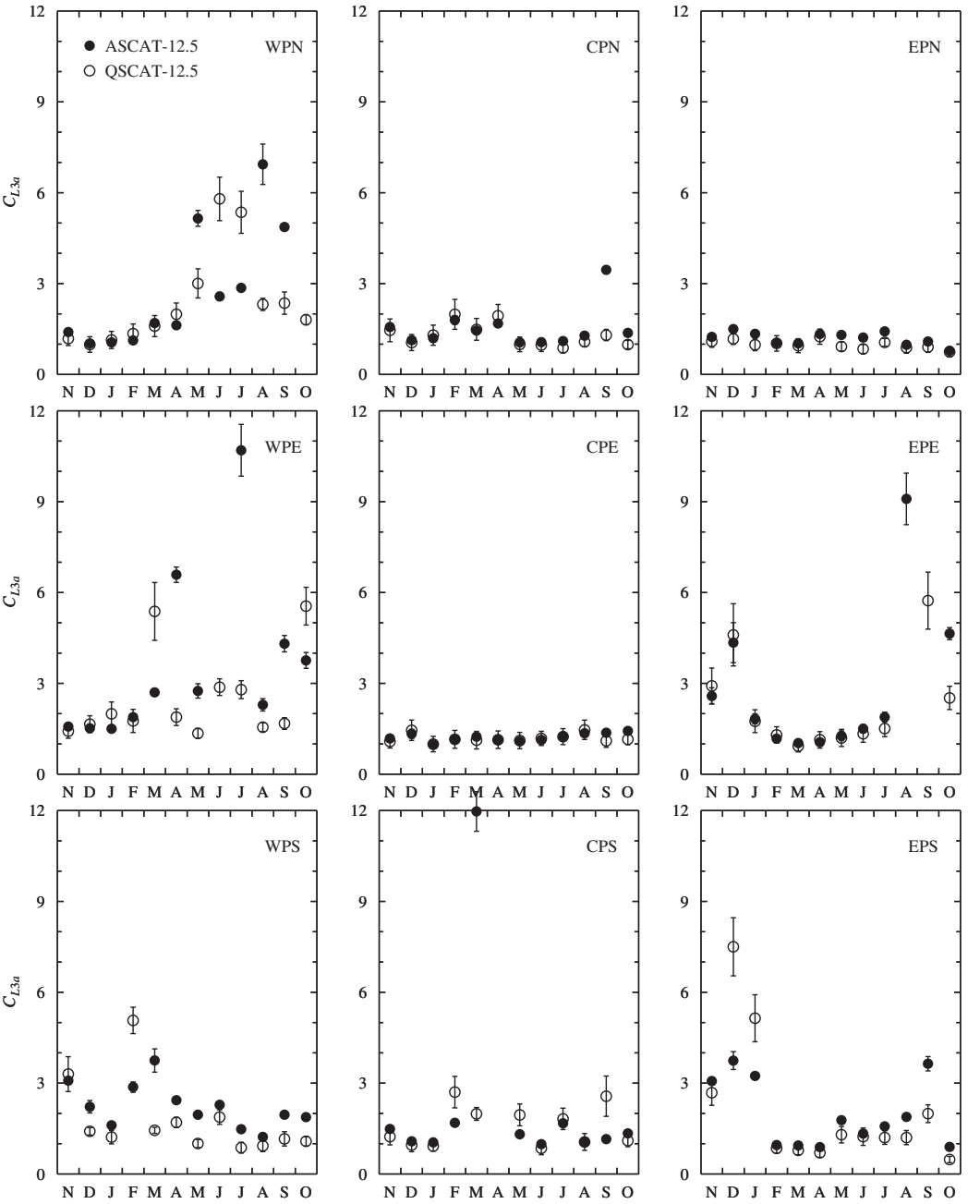

Figure 11. Time series of the Kolmogorov constant C_{L3a} estimated using the energy fluxes shown in Figure 9.

According to turbulence theory, the signature of a 3-D (downscale) cascade is $D_{LLLa} < 0$ with $S_{La} \approx -0.3$, and the signature of a 2-D (upscale) cascade is $D_{LLLa} > 0$ with $S_{La} \approx +0.03$. The question that is typically posed is whether atmospheric kinetic energy cascades downscale or upscale. However, the graphs of $S_{La}(r)$ in Figure 5 and the time series of S_{La} in Figure 6 give evidence that turbulent kinetic energy moves both downscale and upscale, depending on the region and season. These results are reinforced in Figure 9, which shows the Kolmogorov constant estimated using the third-order structure function law (equation (5)): values consistent with 3-D turbulence are found when S_{La} is close to -0.5, and, when S_{La} is near 0, values are increasing or very large, consistent with results from 2-D turbulence studies [*Boffetta et al.*, 2000].

Our results imply that ocean wind turbulence in the tropical Pacific is predominantly downscale but transitions to predominantly upscale when conditions are favorable. The physical picture we propose to account

© 2014. American Geophysical Union. All Rights Reserved.

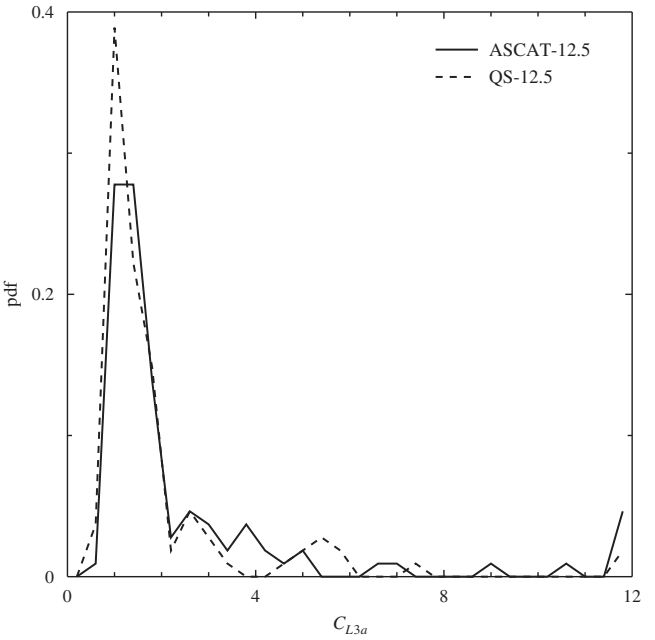

Figure 12. Normalized histograms of the Kolmogorov constant C_{L3a}.

for such a mixture of 3-D and 2-D turbulence is relatively straightforward. Over warm SST air is heated which enhances convection and producing 3-D turbulence. On the other hand, over cool SST air is cooled inhibiting convection and creating conditions favorable for 2-D turbulence. This picture is consistent with results for EPE, where there is a regular seasonal cycle between a warm/wet season and cold season as the ITCZ migrates and modulates the spatial extent of the cold tongue. However, the west Pacific is dominated by very warm SST throughout the year, so it might be surprising that conditions could ever be favorable for anything but 3-D turbulence. But the convection in the west Pacific, especially over the warm pool, produces considerable rainfall. This creates a pool of cool water near the surface, reducing convection and providing conditions favorable for 2-D turbulence. This is consistent with Figures 6 and 9, which indicate 2-D-like turbulence during summer months and 3-D turbulence during winter months.

In this paper, statistical tools from turbulence theory have been applied to scatterometer winds, yielding new insights on the direction of the energy cascade and structure of turbulence in the marine boundary layer. The work also showed that the signature of intense small-scale ($<$100 km) events could be seen in graphs of the skewness, implying that this diagnostic may be useful in the monitoring and study of tropical disturbances. Finally, we emphasize that velocity difference PDFs and their statistics provide a new and powerful approach to compare wind products and diagnose outliers. A vitally important task for the development of high quality records of vector winds spanning many years and different instruments.

Acknowledgments

The ASCAT-12.5 and ASCAT-25 data used in this work can be ordered online from the EUMETSAT Data Centre (http://www.eumetsat.int/website/home/ Data/DataDelivery/EUMETSATDataCentre/ index.html) as OSI SAF data in BUFR or NetCDF format. They can also be ordered from PO.DAAC (http://podaac.jpl.nasa.gov/datasetlist?ids=Sensor& values=ASCAT&search=) in NetCDF format only. The SeaWinds-NOAA and QSCAT-12.5 data are also available from PO.DAAC. The SeaWinds-KNMI data are available from the KNMI archive upon an email request to scat@knmi.nl. Rain-rates were obtained from the Tropical Rainfall Measuring Mission's (TRMM) Microwave Imager (TMI) archive at the Remote Sensing Systems Web site (http://www.ssmi.com). SeaWinds Radiometer (SRAD) rain-rates are included with the QuikSCAT 25 km L2B science data product that is available from PO.DAAC. This work has been funded by EUMETSAT in the context of the NWP SAF part of the SAF network. The contribution of G.P.K. has been supported by EUMETSAT under the visiting scientist programme. G.P.K. wishes to thank George Rowlands and Robert Kerr for useful discussions. The authors also thank David Byrne for his valuable criticisms and suggestions.

References

Antonia, R. A., M. Ould-Rouis, F. Anselmet, and Y. Zhu (1997), Analogy between predictions of Kolmogorov and Yaglom, *J. Fluid Mech.*, *332*, 395–409.

Boffetta, G., and R. E. Ecke (2012), Two-dimensional turbulence, *Annu. Rev. Fluid Mech.*, *44*, 427–451, doi:10.1146/annurev-fluid-120710-101240.

Boffetta, G., A. Celani, and M. Vergassola (2000), Inverse energy cascade in two-dimensional turbulence: Deviations from Gaussian behavior, *Phys. Rev. E*, *61*, R29–R32, doi:10.1103/PhysRevE.61.R29.

Byrne, D., and J. A. Zhang (2013), Height-dependent transition from 3-D to 2-D turbulence in the hurricane boundary layer, *Geophys. Res. Lett.*, *40*, 1439–1442, doi:10.1002/grl.50335.

Charney, J. G. (1971), Geostrophic turbulence, *J. Atmos. Sci.*, *28*, 1087–1095.

Chelton, D. B., M. G. Schlax, M. H. Freilich, and R. F. Milliff (2004), Satellite measurements reveal persistent small-scale features in ocean winds, *Science*, *303*(5660), 978–983, doi:10.1126/science.1091901.

Cho, J. Y. N., and E. Lindborg (2001), Horizontal velocity structure functions in the upper troposphere and lower stratosphere. 1. Observations, *J. Geophys. Res.*, *106*, 10,223–10,232.

Cho, J. Y. N., B. E. Anderson, J. D. W. Barrick, and K. L. Thornhill (2001), Aircraft observations of boundary layer turbulence: Intermittency and the cascade of energy and passive scalar variance, *J. Geophys. Res.*, *106*, 32,469–32,479.

Dewan, E. (1997), Saturated-cascade similitude theory of gravity wave spectra, *J. Geophys. Res.*, *102*, 29,799–29,817.

Dewan, E. M. (1979), Stratospheric wave spectra resembling turbulence, *Science*, *204*, 832–835.

Figa-Saldaña, J., J. Wilson, E. Attema, R. Gelsthorpe, M. Drinkwater, and A. Stoffelen (2002), The advanced scatterometer (ASCAT) on the meteorological operational (MetOp) platform: A follow on for the European wind scatterometers, *Can. J. Remote Sens.*, *28*, 404–412, doi:10.5589/m02-035.

Fore, A., B. Stiles, A. Chau, B. Williams, R. Dunbar, and E. Rodríguez (2013), Point-wise wind retrieval and ambiguity removal improvements for the QuikSCAT climatological data set, *IEEE Trans. Geosci. Remote Sens.*, *52*(1), 51–59, doi:10.1109/TGRS.2012.2235843..

Frisch, U. (1995), *Turbulence: The Legacy of A. N. Kolmogorov*, 296 pp., Cambridge Univ. Press, Cambridge, U. K.

© 2014. American Geophysical Union. All Rights Reserved.

Gage, K. S. (1979), Evidence for a $k^{-5/3}$ law inertial range in mesoscale two-dimensional turbulence, *J. Atmos. Sci.*, *36*, 1950–1954.
Giles, M. J. (1997), Probability distribution functions for small scale turbulence, *Appl. Sci. Res.*, *57*, 223–234, doi:10.1007/BF02506061.
King, G. P., J. Vogelzang, and A. Stoffelen (2015), Second-order structure function analysis of scatterometer winds over the Tropical Pacific, *J. Geophys. Res. Oceans*, *120*, doi:10.1002/2014JC009992.
KNMI (2013), *ASCAT Wind Product User Manual*, EUMETSAT OSI SAF report SAF/OSI/CDOP/KNMI/TEC/MA/126, KNMI, De Bilt, Netherlands. [Available at www.knmi.nl/scatterometer.]
Landau, L. D., and E. M. Lifshitz (1987), *Fluid Mechanics*, Butterworth-Heinemann, London, U. K.
Laupattarakasem, P., W. L. Jones, K. Ahmad, and S. Veleva (2005), Calibration/validation of the Sea/Winds radiometer rain rate algorithm, in *Proceedings of MTS/IEEE OCEANS*, vol. 3, pp. 2601–2604, IEEE, N. Y., doi:10.1109/OCEANS.2005.1640163.
Lilly, D. K. (1983), Stratified turbulence and the mesoscale variability of the atmosphere, *J. Atmos. Sci.*, *40*, 749–761.
Lilly, D. K. (1989), Two-dimensional turbulence generated by energy sources at two scales, *J. Atmos. Sci.*, *46*, 2026–2030.
Lin, W., M. Portabella, A. Stoffelen, A. Turiel, and A. Verhoef (2014), Rain identification in ASCAT winds using singularity analysis, *IEEE Gosci. Remote Sens. Lett.*, *11*(9), 1519–1523, doi:10.1109/LGRS.2014.2298095.
Lindborg, E. (1999), Can the atmospheric kinetic energy spectrum be explained by two-dimensional turbulence?, *J. Fluid Mech.*, *388*, 259–288.
Lindborg, E. (2007), Horizontal wavenumber spectra of vertical vorticity and horizontal divergence in the upper troposphere and lower stratosphere, *J. Atmos. Sci.*, *64*(3), 1017–1025, doi:10.1175/JAS3864.1.
Lindborg, E., and J. Y. N. Cho (2001), Horizontal velocity structure functions in the upper troposphere and lower stratosphere. 2. Theoretical considerations, *J. Geophys. Res.*, *106*, 10,233–10,241.
Lovejoy, S., A. F. Tuck, D. Schertzer, and S. J. Hovde (2009), Reinterpreting aircraft measurements in anisotropic scaling turbulence, *Atmos. Chem. Phys.*, *9*, 5007–5025, doi:10.5194/acp-9-5007-2009.
Lu, C., and S. E. Koch (2008), Interaction of upper-tropospheric turbulence and gravity waves as obtained from spectral and structure function analyses, *J. Atmos. Sci.*, *65*, 2676–2690, doi:10.1175/2007JAS2660.1.
Nastrom, G. D., and K. S. Gage (1985), A climatology of atmospheric wavenumber spectra of wind and temperature observed by commercial aircraft, *J. Atmos. Sci.*, *42*, 950–960.
Nastrom, G. D., K. S. Gage, and W. H. Jasperson (1984), Kinetic energy spectrum of large-and mesoscale atmospheric processes, *Nature*, *310*, 36–38, doi:10.1038/310036a0.
Portabella, M., and A. Stoffelen (2002), A comparison of KNMI quality control and JPL rain flag for SeaWinds, *Can. J. Remote Sens.*, *28*, 424–430.
Portabella, M., and A. Stoffelen (2004), A probabilistic approach for SeaWinds data assimilation, *Q. J. R. Meteorol. Soc.*, *130*(596), 127–159, doi:10.1256/qj.02.205.
Small, R. J., S. deSzoeke, S. Xie, L. O'Neill, H. Seo, Q. Song, P. Cornillon, M. Spall, and S. Minobe (2008), Air-sea interaction over ocean fronts and eddies, *Dyn. Atmos. Oceans*, *45*, 274–319.
Stiles, B., B. Pollard, and R. Dunbar (2002), Direction interval retrieval with thresholded nudging: A method for improving the accuracy of QuikSCAT winds, *IEEE Trans. Geosci. Remote Sens.*, *40*, 79–89.
Stoffelen, A., and M. Portabella (2006), On Bayesian scatterometer wind inversion, *IEEE Trans. Geosci. Remote Sens.*, *44*(6), 1523–1533, doi:10.1109/TGRS.2005.862502.
Tsai, W.-T., M. Spencer, C. Wu, C. Winn, and K. Kellogg (2000), SeaWinds on QuikSCAT: Sensor description and mission overview," Geoscience and Remote Sensing Symposium. In *Proceedings IGARSS 2000*. IEEE 2000 International, vol. 3, pp. 1021–1023, doi:10.1109/IGARSS.2000.858008.
Van Zandt, T. E. (1982), A universal spectrum of buoyancy waves in the atmosphere, *Geophys. Res. Lett.*, *9*, 575–578.
Vogelzang, J., A. Stoffelen, A. Verhoef, J. de Vries, and H. Bonekamp (2009), Validation of two-dimensional variational ambiguity removal on SeaWinds scatterometer data, *J. Atmos. Oceanic Technol.*, *26*, 1229–1245, doi:10.1175/2008JTECHA1232.1.
Vogelzang. J., A. Stoffelen, A. Verhoef, and J. Figa-Saldaña (2011), On the quality of high-resolution scatterometer winds, *J. Geophys. Res.*, *116*, C10033, doi:10.1029/2010JC006640.
Wyrtki, K. (1989), Some thoughts about the west Pacific warm pool, in *Proceedings of the Western Pacific International Meeting and Workshop on TOGA COARE*, edited by J. Picaut, R. Lucas, and T. Delcroix, pp. 99–109, ORSTUM, Cent. de Nouma, New Caledonia, N. Z.
Xia, H., M. Shats, and G. Falkovich (2009), Spectrally condensed turbulence in thin layers, *Phys. Fluids*, *21*, 125,101, doi:10.1063/1.3275861.
Yakhot, V. (1999), Two-dimensional turbulence in the inverse cascade range, *Phys. Rev. E*, *60*, 5544–5551, doi:10.1103/PhysRevE.60.5544.

© 2014. American Geophysical Union. All Rights Reserved.